

Time-dependent Kelvin cat-eye structure due to current–topography interaction

Marcelo V. Flamarion¹, André Nachbin^{2,†} and Roberto Ribeiro-Jr.³

¹UFRPE/Rural Federal University of Pernambuco, UACSA/Unidade Acadêmica do Cabo de Santo Agostinho, BR 101 Sul, 5225, Ponte dos Carvalhos, Cabo de Santo Agostinho, PE, 54503-900, Brazil

²IMPA/National Institute of Pure and Applied Mathematics, Est. D. Castorina, 110, Rio de Janeiro, RJ, 22460-320, Brazil

³UFPR/Federal University of Paraná, Departamento de Matemática, Centro Politécnico, Jardim das Américas, Caixa Postal 19081, Curitiba, PR, 81531-980, Brazil

(Received 13 May 2019; revised 23 December 2019; accepted 13 January 2020)

Non-stationary, rotational, linear surface waves are considered where the underlying sheared current has constant vorticity. A time-dependent study is presented on the formation and persistence of a Kelvin cat-eye structure in the presence of bottom topography. The flow domain is two-dimensional, which allows for the use of a conformal mapping and working in a computational flat-bottom domain. In some cases an initial disturbance is prescribed, while in others the waves are generated from rest. Submarine particle dynamics numerically captures the horizontal critical layer, defined by closed orbits separating the fluid domain into two disjoint regions. In the wave's moving frame, these recirculation regions are structured in the form of Kelvin cat-eyes. Owing to the interaction with topography, the usual travelling-wave formulation is abandoned and the critical layer is identified through a non-stationary set of equations. The respective time-dependent Kelvin cat-eye structure dynamically adjusts itself at the onset of wave–topography interaction, without losing its integrity. The formation of a Kelvin cat-eye structure is also studied in the case where the surface is initially undisturbed. Surface waves are generated from either the current–topography interaction or by a pressure distribution suddenly imposed along the free surface. Under the pressure forcing, an isolated cat-eye forms with a single recirculation region beneath the wave.

Key words: surface gravity waves, critical layers

1. Introduction and background

Water waves propagating in the presence of a background flow is a problem of great current interest regarding both applications as well as the mathematical questions that arise. This topic is broad and therefore it is difficult to give a comprehensive overview of contributions. For the interested reader, we mention

† Email address for correspondence: nachbin@impa.br

a few recent references from which the bibliography may be useful. Regarding geophysical applications, Soontiens, Subich & Stastna (2010) studied trapped internal waves over isolated topography, in the presence of a background shear. The book by Buhler (2009) presents several techniques relevant to geophysical fluid dynamics, where an example includes ‘the interplay between large-scale Rossby waves and two-dimensional turbulence’. At the other extreme of the scientific spectrum, we have many contributions in analysis with rigorous theoretical results on the existence of surface waves in the presence of vorticity, namely rotational waves as defined by several authors (Ko & Strauss 2008; Wahlén 2009; Ehrnström, Escher & Villari 2012). Problems include the existence of stagnation points in the wave’s moving frame, in identifying Kelvin cat-eye recirculation regions and the respective critical layer below nonlinear (periodic, travelling) Stokes waves, among others. The first rigorous construction for linear (constant-vorticity) rotational waves, and one critical layer, was done by Wahlén (2009). The important first step studying linear waves was based on the work by Ehrnström & Villari (2008). Later these two authors, in collaboration with Escher, constructed the first waves with several (arbitrarily many) critical layers (see Ehrnström *et al.* 2012). A recent work on rotational steady waves and critical layers is presented by Aasen & Varholm (2018), with small-amplitude waves and an affine vorticity. These authors mention that, besides difficulties regarding the mathematical analysis, there are ‘many physical effects that can induce rotation in waves, such as wind and thermal or salinity gradients, and rotational waves are also important in wave–current interactions’. Many other recent references on nonlinear rotational waves may be found through Constantin (2011), Henry (2013), Constantin, Strauss & Varvaruca (2016) and Constantin (2017), among others.

Numerical studies with travelling waves and the respective stationary submarine structures, such as stagnation points, started with the work of Teles da Silva & Peregrine (1988). More detailed numerical studies on the flow structure beneath travelling waves appeared recently, as for example that of Vasan & Oliveras (2014) and Ribeiro-Jr., Milewski & Nachbin (2017). A numerical stability study for finite-amplitude steady rotational surface waves is presented by Francius & Kharif (2017).

Having travelling waves in mind, most studies are formulated in the wave’s moving frame, thus addressing stationary differential equations. In this case particle pathlines can be visualized through the level curves of the streamfunction. In certain regimes the particle dynamics form a critical layer. In the literature the definition of a critical layer has a few non-conflicting variations, as seen in Ehrnström *et al.* (2012) and Constantin *et al.* (2016). The former is better suited for our non-stationary recirculation regions. Ehrnström *et al.* (2012, p. 407) define a critical layer as a horizontal layer with closed streamlines separating the fluid into two disjoint regions. The closed streamline regions are structured in the Kelvin cat-eye pattern. Here we adopt a similar definition, where we replace streamlines by pathlines (particle paths), since our particle dynamics is non-autonomous.

As mentioned above, the linear wave regime is a first step in a topic not much explored theoretically and numerically. The nonlinear regime is certainly of interest. Unfortunately, for nonlinear travelling waves, there is strong evidence of instabilities, some associated with the Benjamin–Feir modulational instability (Francius & Kharif 2017). To the best of our knowledge there are no articles with time-dependent potential theory models and non-stationary waves studying the submarine Kelvin cat-eye structure and the associated critical layer for the Euler equations, even in the linear regime. However, for reduced models, such as the Korteweg–de Vries (KdV)

equation with uniform depth, an asymptotic study was done by Johnson (1986). Under a specific vorticity distribution, with the inclusion of a vortex sheet, Johnson analysed the development of a critical layer under a two-soliton solution. Of particular interest, Johnson (1986, figure 7) illustrates schematically the ‘birth process’ (as this author calls it) of a Kelvin cat-eye as a consequence of a stagnation point in the wave’s moving frame. The physical mechanism relates to this stagnation point, which creates a ‘region which can support closed streamlines’, as mentioned by Johnson (1986). In a later paper, Ehrnström & Villari (2008) comment that the presence of vorticity – even when it is constant – changes the particle trajectories in a qualitative way: the presence of a point with the wave speed defines a vortex in the wave’s moving frame.

We remove the restriction of travelling waves, and our propagating waves might change their profiles as time evolves, implying that the streamlines are no longer pathlines. In this case, not only do we have to compute the free surface conditions in time, but also we have to solve the particle trajectories’ dynamical system for a cloud of tracers in order to visualize the pathlines and the respective Kelvin cat-eye submarine structure.

The persistence of the Kelvin cat-eye structure is first tested through a conveniently chosen initial surface disturbance, which eventually interacts with the bottom topography. We consider a modulated initial surface disturbance, with a Kelvin cat-eye structure already present at time $t = 0$. This wavetrain is chosen so that dispersive effects are very weak and we observe effectively (namely, to a good approximation) a wave of translation. The persistence of the cat-eye structure is very clear when observed through a cloud of tracers, even in the presence of the topographic forcing. The recirculation region adjusts itself to the topographic undulations.

Our novel results on Kelvin cat-eye formation are obtained by letting linear surface waves be generated from rest. The free surface is initially undisturbed. The onset of surface-wave generation starts through the current–topography interaction, or by a localized (steady) surface pressure distribution suddenly applied at time $t = 0^+$. This case is motivated by the work of Johnson (2012). A localized low-pressure forcing is applied where subsequently a stationary pulse forms, together with two depression pulses propagating in opposite directions. An isolated Kelvin cat-eye then forms under the stationary pulse. These time-dependent Kelvin cat-eye structures and the associated critical-layer scenarios described above have not been contemplated in the literature.

The paper is organized as follows. In § 2 we present the mathematical formulation of the linear free surface Euler equations in the canonical domain, which is a uniform strip where computations are more easily performed, as depicted to the right in figure 1. The canonical domain is defined through a conformal mapping. In § 3 the numerical method is presented. We introduce the dynamical system for particle trajectories in canonical coordinates. By not using a travelling-wave formulation, this dynamical system is no longer autonomous and its vector field must be constantly updated. This update depends on solutions of the Euler equations and is done through the potential component of the velocity field. Properties of harmonic functions are used in order to write all ‘Euler information’ needed in terms of one-dimensional Fourier expressions. These are essentially Fourier-type operators acting on the Dirichlet (boundary) data. This framework leads to the numerical method described in § 3. The results are presented in § 4 and the conclusions in § 5.

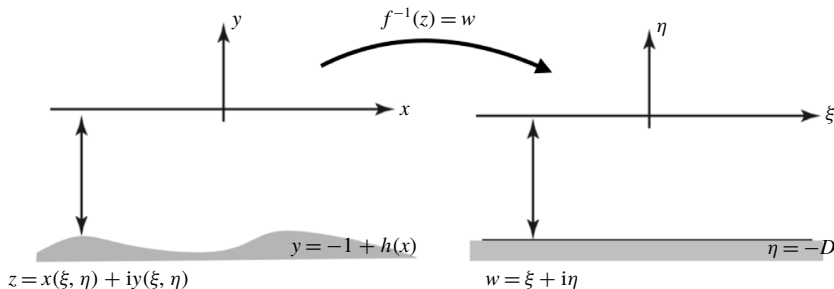


FIGURE 1. The inverse conformal mapping. The bottom topography is flattened out in the canonical domain.

2. Mathematical formulation

We have a two-dimensional incompressible flow of an inviscid fluid. The corresponding formulation presented in Flamarion, Milewski & Nachbin (2019) starts with the Euler equations, which are then written in potential theory form. We here summarize the formulation, recalling that it is convenient to first start by considering that the bottom obstacle or the surface pressure distribution are moving with uniform speed U_0 . With this in mind, we write the velocity field in the form

$$(u, v) = \nabla \tilde{\varphi} + (ay, 0), \tag{2.1}$$

where $\tilde{\varphi}(x, y, t)$ is the velocity potential of the irrotational component of the flow, while $-a$ prescribes constant vorticity. Potential theory formulation yields

$$\begin{aligned} \Delta \tilde{\varphi} &= 0, & \text{for } -h_0 + h(x + U_0t) < y < \tilde{\zeta}(x, t), \\ (U_0 - ah_0)h_x + ah h_x + \tilde{\varphi}_x h_x &= \tilde{\varphi}_y, & \text{at } y = -h_0 + h(x + U_0t), \\ \tilde{\zeta}_t + (a\tilde{\zeta} + \tilde{\varphi}_x)\tilde{\zeta}_x - \tilde{\varphi}_y &= 0, & \text{at } y = \tilde{\zeta}(x, t), \\ \tilde{\varphi}_t + \frac{1}{2}(\tilde{\varphi}_x^2 + \tilde{\varphi}_y^2) + a\tilde{\zeta}\tilde{\varphi}_x + \tilde{\zeta} - a\tilde{\psi} &= -\frac{\tilde{P}(x + U_0t)}{\rho}, & \text{at } y = \tilde{\zeta}(x, t), \end{aligned}$$

where $\tilde{\zeta}(x, t)$ is the wave elevation and $\tilde{\psi}$ is the harmonic conjugate of $\tilde{\varphi}$. The applied pressure distribution is denoted by \tilde{P} and the bottom profile by h . In a moving frame, given by $x \rightarrow x + U_0t$, and denoting $\tilde{\zeta}(x, t) \equiv \zeta(x + U_0t, t)$, $\tilde{\varphi}(x, y, t) \equiv \phi(x + U_0t, y, t)$, these equations read as

$$\left. \begin{aligned} \Delta \phi &= 0 & \text{for } -h_0 + h(x) < y < \zeta(x, t), \\ (U_0 - ah_0)h_x + ah h_x + \phi_x h_x &= \phi_y & \text{at } y = -h_0 + h(x), \\ \zeta_t + (U_0 + a\zeta + \phi_x)\zeta_x - \phi_y &= 0 & \text{at } y = \zeta(x, t), \\ \phi_t + \frac{1}{2}(\phi_x^2 + \phi_y^2) + (U_0 + a\zeta)\phi_x + \zeta - a\psi &= -\frac{P(x)}{\rho} & \text{at } y = \zeta(x, t). \end{aligned} \right\} \tag{2.2a-d}$$

In this framework we have a background sheared current satisfying the Neumann condition around a stationary obstacle along the bottom. The surface pressure distribution is also stationary in this reference frame.

Next we write the system in dimensionless form. In the framework above, we have a fluid, of constant density ρ , flowing with a background sheared current, which varies

vertically as $ay + U_0$. The depth variations of the channel are defined at the bottom boundary as $y = -h_0 + h(x)$, where the undisturbed depth is h_0 while $h(x)$ describes the topography's profile. As our characteristic scales for length, speed, time and pressure we choose the quantities h_0 , $(gh_0)^{1/2}$, $(h_0/g)^{1/2}$ and ρgh_0 . The dimensionless velocity field (u, v) reads

$$(u, v) = \nabla \bar{\phi} + (\Omega y + F, 0), \tag{2.3}$$

where we have the Froude number $F = U_0/(gh_0)^{1/2}$, the dimensionless vorticity $\omega = -\Omega = ah_0/(gh_0)^{1/2}$, and g is the acceleration due to gravity. The dimensionless, linearized equations are

$$\left. \begin{aligned} \Delta \bar{\phi} &= 0, & \text{for } -1 + h(x) < y < 0, \\ (F - \Omega)h_x + \Omega h h_x + \bar{\phi}_x h_x &= \bar{\phi}_y, & \text{at } y = -1 + h(x), \\ \bar{\zeta}_t + F \bar{\zeta}_x &= \bar{\phi}_y, & \text{at } y = 0, \\ \bar{\phi}_t + F \bar{\phi}_x + \bar{\zeta} - \Omega \bar{\psi} &= -P(x), & \text{at } y = 0. \end{aligned} \right\} \tag{2.4a-d}$$

We omit the bars for h and P , which are now dimensionless. For simplicity, from now on, each time we mention the Euler equations we mean the linear system (2.4).

Regardless of working with linear or nonlinear waves, the particle trajectory beneath a surface wave is governed by the dynamical system

$$\left. \begin{aligned} \frac{dx}{dt} &= \bar{\phi}_x + \Omega y + F, \\ \frac{dy}{dt} &= \bar{\phi}_y, \\ x(0) &= x_0, \quad y(0) = y_0. \end{aligned} \right\} \tag{2.5a-c}$$

To compute its vector field, one needs $\bar{\phi}_x$ and $\bar{\phi}_y$ in the bulk of the fluid. These are obtained from the Euler equations (2.4). From the dispersion relation of system (2.4), we have that the linear wave speed c is given by

$$c = F - \frac{\Omega \tanh(k)}{2k} \pm \frac{\sqrt{\Omega^2 \tanh^2(k) + 4k \tanh(k)}}{2k}. \tag{2.6}$$

We will consider the mode with the positive sign of the square root. In the presence of a background flow, there is some ambiguity in the choice of the wave speed. The choice made, through expression (2.6), is with reference to the Froude number. For clarity, F is the (dimensionless) surface speed of the background flow. In the simplified case that $\Omega = 0$, we have $c = F \pm (\tanh(k)/k)^{1/2}$, the latter being the phase speed.

Suppose we have a wave solution in a moving frame of the form $\bar{\phi}(x, y, t) = \tilde{\phi}(x - ct, y, t)$. If $(x(t), y(t))$ represents a particle trajectory given by the dynamical system (2.5), then, in the wave's moving frame $X = x - ct$ and $Y = y$, the trajectories $(X(t), Y(t))$ satisfy the dynamical system in the form

$$\left. \begin{aligned} \frac{dX}{dt} &= \tilde{\phi}_X(X, Y, t) + \Omega Y + F - c = \tilde{\psi}_Y(X, Y, t) + \Omega Y + F - c, \\ \frac{dY}{dt} &= \tilde{\phi}_Y(X, Y, t) = -\tilde{\psi}_X(X, Y, t). \end{aligned} \right\} \tag{2.7a,b}$$

As mentioned above, this system of ordinary differential equations (ODEs) is nonlinear even for a linear wave with no background flow. The vector field of this ODE depends on the solution of the linear potential theory (Euler) equations. A second linearization, as for example by expanding the potential in X and Y , can lead to closed elliptical orbits. This is further discussed in Constantin & Villari (2008).

From (2.6) and (2.7) it is easy to show that we cannot have waves excessively long ($k \rightarrow \infty$) while seeking a Kelvin cat-eye structure. This conclusion arises from the relation

$$Y^* = -\frac{\tanh(k)}{2k} \pm \sqrt{\frac{\tanh^2(k)}{4k^2} + \frac{\tanh(k)}{\Omega^2 k}}, \tag{2.8}$$

where Y^* is the depth of the stagnation point. As mentioned in the Introduction and discussed by Johnson (1986), for the cat-eye structure to exist, one needs the presence of stagnation points, in the wave’s moving frame. For linear waves, the stagnation point will appear as a balance between wavelength, total depth and the vorticity applied. Having in mind (2.8) and as defined through (2.3), we adopt a background velocity profile given by $U(y) = (\Omega y + F, 0)$.

In the next section we detail the conformal mapping technique for solving the Euler equations (2.4) and the dynamical system (2.5) or (2.7) in the canonical domain, where we have a flat strip.

2.1. Conformal mapping

As depicted in figure 1, the conformal mapping $z=f(w)$ from the canonical domain (a flat strip) onto the physical domain is defined by

$$z(\xi, \eta) = x(\xi, \eta) + iy(\xi, \eta),$$

where in the canonical w -plane $w = \xi + i\eta$. We have the following boundary conditions:

$$y(\xi, 0) = 0 \quad \text{and} \quad y(\xi, -D) = -1 + H(\xi).$$

We are imposing that the canonical upper boundary $\eta = 0$ is mapped onto the undisturbed free surface $y = 0$. We denote by $H(\xi) = h(x(\xi, -D))$ the topography representation in the ξ -variable, running along the bottom of the flat strip. The flat bottom boundary $\eta = -D$ in the canonical domain is mapped onto the topography profile, which in the physical domain reads as $-1 + h(x)$. The conformal mapping allows for the constant D to be chosen given the constraint that the physical domain has the same length as the canonical domain. Therefore, wavelengths will not be rescaled under the mapping.

We denote by $X(\xi)$ and $Y(\xi)$ the traces of the respective harmonic functions along $\eta = 0$, and by $X_b(\xi)$ the respective trace along the bottom $\eta = -D$. The L -periodic harmonic function y satisfies

$$\begin{aligned} y_{\xi\xi} + y_{\eta\eta} &= 0, & \text{in } -D < \eta < 0, \\ y &= 0, & \text{at } \eta = 0, \\ y &= -1 + H(\xi), & \text{at } \eta = -D. \end{aligned}$$

Using a Fourier transform F in the ξ -variable, we have that

$$y(\xi, \eta) = F_{k \neq 0}^{-1} \left[\frac{-\coth(kD) \sinh(k\eta) \widehat{H}}{\cosh(kD)} \right] + \frac{\eta(1 - \widehat{H}(0))}{D}, \tag{2.9}$$

where $k = (2\pi/L)j$, $j \in \mathbb{Z}$, and

$$F_k[g(\xi)] = \hat{g}(k) = \frac{1}{L} \int_{-L/2}^{L/2} g(\xi)e^{-ik\xi} d\xi,$$

$$F^{-1}[\hat{g}(k)](\xi) = g(\xi) = \sum_{j=-\infty}^{\infty} \hat{g}(k)e^{ik\xi}.$$

The Cauchy–Riemann equation $x_\xi = y_\eta$ yields

$$x(\xi, \eta) = F_{k \neq 0}^{-1} \left[\frac{i \coth(kD) \cosh(k\eta)\hat{H}}{\cosh(kD)} \right] + \frac{1 - \hat{H}(0)}{D} \xi. \tag{2.10}$$

From (2.10) we obtain

$$X_b(\xi) = x(\xi, -D) = F_{k \neq 0}^{-1} [i \coth(kD)\hat{H}] + \frac{1 - \hat{H}(0)}{D} \xi.$$

Again by the Cauchy–Riemann equation $x_\xi = y_\eta$ and (2.9), we obtain an alternative (and equivalent) expression:

$$X_b(\xi) = \frac{1 - \hat{H}(0)}{D} \xi + F^{-1} \left[\frac{i \coth(kD)\hat{H}}{\cosh^2(kD)} \right] + F^{-1} [i \tanh(kD)\hat{H}]. \tag{2.11}$$

As mentioned, we have made the choice that both the canonical and physical domains have the same length. Under this constraint, we now compute the canonical depth D . Let L and λ be the respective lengths, so that

$$X(\xi = L/2) - X(\xi = -L/2) = \lambda$$

with

$$\langle X_\xi \rangle \equiv \frac{1}{L} \int_{-L/2}^{L/2} X_\xi(\xi) d\xi = 1. \tag{2.12}$$

From (2.10) and $\langle X_\xi \rangle = \widehat{X}_\xi(0)$, it follows that

$$1 = \frac{\lambda}{L} = \frac{1 - \hat{H}(0, t)}{D}, \quad \text{where } D = 1 - \langle H \rangle. \tag{2.13}$$

This is the depth of the canonical channel.

The velocity potential ϕ is a harmonic function in both domains. Changing variables in the bottom boundary condition (2.4b) yields the elliptic problem

$$\begin{aligned} \phi_{\xi\xi} + \phi_{\eta\eta} &= 0, & \text{in } -D < \eta < 0, \\ \phi &= \Phi(\xi, t), & \text{at } \eta = 0, \\ \phi_\eta &= (F - \Omega)H_\xi(\xi) + \Omega HH_\xi(\xi), & \text{at } \eta = -D. \end{aligned}$$

The notation is such that $\phi(\xi, \eta, t) \equiv \bar{\phi}(x(\xi, \eta), y(\xi, \eta), t)$ and $\psi(\xi, \eta, t) \equiv \bar{\psi}(x(\xi, \eta), y(\xi, \eta), t)$ is the harmonic conjugate expressed in the canonical domain. Their traces along $\eta = 0$ are denoted by $\Phi(\xi, t)$ and $\Psi(\xi, t)$, respectively. These

time-dependent traces will be updated through the free surface conditions. The harmonic conjugate ψ satisfies

$$\begin{aligned} \psi_{\xi\xi} + \psi_{\eta\eta} &= 0, \quad \text{in } -D < \eta < 0, \\ \psi &= \Psi(\xi, t), \quad \text{at } \eta = 0, \\ \psi &= -(F - \Omega)H(\xi) - \frac{\Omega}{2}H^2(\xi) + Q, \quad \text{at } \eta = -D, \end{aligned}$$

where $Q = Q(t)$. Solving these elliptic problems in Fourier space leads to

$$\left. \begin{aligned} \phi(\xi, \eta, t) &= \mathbf{F}^{-1} \left[\frac{\cosh(k(\eta + D))}{\cosh(kD)} \widehat{\Phi}(k, t) + \left(\frac{i(F - \Omega)\widehat{H} + i\frac{\Omega}{2}\widehat{H}^2}{\cosh(kD)} \right) \sinh(k\eta) \right], \\ \psi(\xi, \eta, t) &= \mathbf{F}^{-1} \left[\left(\widehat{\Psi}(k, t) + \frac{(F - \Omega)\widehat{H} + \frac{\Omega}{2}\widehat{H}^2}{\cosh(kD)} \right) \frac{\sinh(k(D + \eta))}{\sinh(kD)} \right. \\ &\quad \left. - \left(\frac{(F - \Omega)\widehat{H} + \frac{\Omega}{2}\widehat{H}^2}{\cosh(kD)} \right) \cosh(k\eta) \right] - \frac{Q(t)}{D} \eta. \end{aligned} \right\} \tag{2.14a,b}$$

In order to find $Q(t)$, we start with the Cauchy–Riemann equation $\psi_\eta = \phi_\xi$ and use the periodicity in ξ to obtain

$$\widehat{\psi}_\eta(k=0, \eta, t) = \widehat{\phi}_\xi(k=0, \eta, t) = \frac{1}{L} \int_{-L/2}^{L/2} \phi_\xi(\xi, \eta, t) \, d\xi = 0.$$

From (2.14b) we have

$$\begin{aligned} \psi_\eta(\xi, \eta, t) &= \mathbf{F}^{-1} \left[\left(\widehat{\Psi}(k, t) + \frac{(F - \Omega)\widehat{H} + \frac{\Omega}{2}\widehat{H}^2}{\cosh(kD)} \right) \frac{k \cosh(k(D + \eta))}{\sinh(kD)} \right. \\ &\quad \left. - \left(\frac{(F - \Omega)\widehat{H} + \frac{\Omega}{2}\widehat{H}^2}{\cosh(kD)} \right) k \sinh(k\eta) \right] - \frac{Q}{D}. \end{aligned}$$

Imposing $\langle \psi_\eta \rangle = 0$ in the equation above yields

$$\left(\widehat{\Psi}(0, t) + (F - \Omega)\widehat{H}(0) + \frac{\Omega}{2}\widehat{H}^2(0) \right) \frac{1}{D} - \frac{Q}{D} = 0,$$

which is rewritten as

$$Q(t) = \widehat{\Psi}(0, t) + (F - \Omega)\widehat{H}(0) + \frac{\Omega}{2}\widehat{H}^2(0).$$

Using $-\phi_\eta = \psi_\xi$ in (2.14), and evaluating over $\eta = 0$, gives

$$\Phi_\xi(\xi, t) = \mathbf{F}^{-1} \left[-i \coth(kD) \left(\widehat{\Psi}_\xi(k, t) + \frac{(F - \Omega)\widehat{H}_\xi + \frac{\Omega}{2}\partial_\xi \widehat{H}^2}{\cosh(kD)} \right) \right]. \tag{2.15}$$

In a similar fashion as presented in Nachbin (2003), the kinematic condition and Bernoulli law are given in the canonical variables. From the Euler equations (2.4) we have that

$$\left. \begin{aligned} N_t &= -\frac{F}{M(\xi)}N_\xi - \frac{\Psi_\xi}{M(\xi)^2}, \\ \Phi_t &= -M(\xi)N - \frac{F}{M(\xi)}\Phi_\xi + \Omega\Psi - P(X(\xi)). \end{aligned} \right\} \tag{2.16a,b}$$

Here $N(\xi, t)$ is the wave elevation in the canonical domain. Through the conformal mapping we have the functional relation $\bar{\zeta}(X(\xi), t) = y(\xi, N(\xi, t))$ between the two wave elevation representations. The mapping's Jacobian, evaluated along the free surface, is denoted as $J(\xi, 0) = X_\xi^2(\xi) \equiv M(\xi)^2$. As in Nachbin (2003), it is convenient to map a reflected domain about the undisturbed free surface $\eta = 0$. This leads to an odd extension of the harmonic function $y(\xi, \eta)$ within the enlarged strip $-D < \eta < D$. This domain reflection is useful in the weakly nonlinear regime where using a Taylor series expansion in the vertical direction yields, to leading order,

$$\bar{\zeta}(X(\xi), t) = y(\xi, N(\xi, t)) \approx M(\xi)N(\xi, t). \tag{2.17}$$

We are in position to rewrite the two-dimensional Euler equations only in the canonical variable ξ . The dependence on the η -variable is implicitly built-in through the harmonic extension performed by the (Hilbert-type) Fourier operator containing $\coth(kD)$ as a multiplier. These operators are defined below. The two-dimensional Euler system is recast in the form

$$\left. \begin{aligned} X_\xi &= 1 + C_{k \neq 0} \left[\mathbf{F}^{-1} \left[\frac{\widehat{H}_\xi}{\cosh(kD)} \right] \right], \\ \Phi_\xi &= -C \left[\widehat{\Psi}_\xi(k, t) + \mathbf{F}^{-1} \left[\frac{(F - \Omega)\widehat{H}_\xi + \frac{\Omega}{2}\partial_\xi \widehat{H}^2}{\cosh(kD)} \right] \right], \\ N_t &= -\frac{F}{M(\xi)}N_\xi - \frac{\Psi_\xi}{M(\xi)^2}, \\ \Phi_t &= -M(\xi)N - \frac{F}{M(\xi)}\Phi_\xi + \Omega\Psi - P(X(\xi)), \end{aligned} \right\} \tag{2.18a-d}$$

where

$$\left. \begin{aligned} H(\xi) &= h(X_b(\xi)), \\ X_b(\xi) &= \xi + C_{k \neq 0} \left[\mathbf{F}^{-1} \left[\frac{\widehat{H}}{\cosh^2(kD)} \right] \right] + \mathbf{F}^{-1}[i \tanh(kD)\widehat{H}]. \end{aligned} \right\} \tag{2.19a,b}$$

The Fourier operators are:

$$C[\cdot] \equiv \mathbf{F}^{-1}[i \coth(kD)\mathbf{F}_k[\cdot]] \quad \text{and} \quad C_{k \neq 0}[\cdot] \equiv \mathbf{F}^{-1}[i \coth(kD)\mathbf{F}_{k \neq 0}[\cdot]].$$

3. Numerical method

Our main goal in this study is to exhibit (numerically) the formation from rest of a Kelvin cat-eye structure, as well as its persistence while overcoming a bottom topography. In the stationary wave regime, particle pathlines coincide with streamlines. In the non-stationary regime, in order to display the evolution in time of the Kelvin cat-eye structure, we compute the orbits (pathlines) of several particles. These tracers will enable the time-dependent visualization of the critical layer. Owing to the presence of bottom topography, the wave and particle dynamics are computed in the (simpler) canonical domain and then mapped back onto the physical domain for a proper visualization of the pathlines.

In order to describe our numerical procedure, the Euler formulation, presented earlier, is now coupled with the tracer dynamics. Recall that particle orbits $(x(t), y(t))$ are governed by system (2.5). In the canonical domain the pre-image of a trajectory is given by $(\xi(t), \eta(t))$, where the mapping onto the physical domain yields $(\tilde{x}(t), \tilde{y}(t)) = (x(\xi(t), \eta(t)), y(\xi(t), \eta(t)))$. The dynamical system for computing the particle pathlines in the canonical domain is

$$\left. \begin{aligned} \frac{d\xi}{dt}(t) &= \frac{\phi_\xi(\xi, \eta, t)}{J(\xi, \eta)} + \frac{(\Omega y(\xi, \eta) + F)x_\xi(\xi, \eta)}{J(\xi, \eta)}, \\ \frac{d\eta}{dt}(t) &= \frac{\phi_\eta(\xi, \eta, t)}{J(\xi, \eta)} - \frac{(\Omega y(\xi, \eta) + F)y_\xi(\xi, \eta)}{J(\xi, \eta)}, \\ \xi(0) &= \xi_0, \quad \eta(0) = \eta_0. \end{aligned} \right\} \quad (3.1a-c)$$

The Jacobian is expressed as $J(\xi, \eta) = x_\xi^2(\xi, \eta) + y_\xi^2(\xi, \eta)$. The particle is initially located at (ξ_0, η_0) , the pre-image of (x_0, y_0) . The physical pathline is obtained from

$$\tilde{x}(t) = x(\xi(t), \eta(t)) = \mathbf{F}_{k \neq 0}^{-1} \left[\frac{i \coth(kD) \cosh(k\eta) \widehat{H}}{\cosh(kD)} \right] + \frac{1 - \widehat{H}(0)}{D} \xi, \quad (3.2)$$

$$\tilde{y}(t) = y(\xi(t), \eta(t)) = \mathbf{F}_{k \neq 0}^{-1} \left[\frac{-\coth(kD) \sinh(k\eta) \widehat{H}}{\cosh(kD)} \right] + \frac{\eta(1 - \widehat{H}(0))}{D}. \quad (3.3)$$

Recall that in the canonical variables the topography is denoted by $-1 + H(\xi)$. All Fourier transforms \mathbf{F} are in the ξ -variable, computed numerically through a fast Fourier transform (FFT). In computing the vector field of the dynamical system (3.1) we use the potential ϕ given by its Fourier representation

$$\phi(\xi, \eta, t) = \mathbf{F}^{-1} \left[\frac{\cosh(k(\eta + D))}{\cosh(kD)} \widehat{\Phi}(k, t) + \left(\frac{i(F - \Omega)\widehat{H} + i\frac{\Omega}{2}\widehat{H}^2}{\cosh(kD)} \right) \sinh(k\eta) \right]. \quad (3.4)$$

The dynamical system is not autonomous. Therefore, its vector field is updated through the free surface conditions (2.16).

In other words, we evolve the boundary data for the velocity potential as well as for the wave profile. Within the fluid body, updated values of ϕ and its derivatives are readily available from expression (3.4). The boundary data of its harmonic conjugate are obtained from

$$\widehat{\Psi}(k, t) = i \tanh(kD) \widehat{\Phi}(k, t) - \left(\frac{(F - \Omega)\widehat{H} + \frac{\Omega}{2}\widehat{H}^2}{\cosh(kD)} \right). \quad (3.5)$$

The term $P(X)$, in the dynamic condition (2.16*b*), is only used when a pressure distribution is considered along the free surface. We use the fourth-order Runge–Kutta method (RK4) for numerically evolving systems (3.1) and (2.16). In Nachbin & Ribeiro-Jr. (2017) a review is presented on some aspects of the numerical methodology. In particular, the RK4 method was thoroughly tested for submarine particle dynamics, exhibiting very high precision in capturing closed orbits in the case of a uniform current. In Flamarion *et al.* (2019) the RK4 scheme was tested for wave generation with both a KdV model and the potential theory model. In the long-wave regime the two solutions agreed very well.

As mentioned, all Fourier transforms are approximated by the FFT on a uniform grid, with all derivatives performed in Fourier space (Milewski & Tabak 1999; Trefethen 2001). The computational grid in the canonical domain is given by $\xi \in [-L/2, L/2)$, with N uniformly spaced points, with grid size $\Delta\xi = L/N$. This corresponds to a non-uniform grid in physical space. A typical resolution has $N = 2^{13}$ with a time step $\Delta t = 0.05$. A Kelvin cat-eye structure is typically captured with a cloud of 90 tracers.

We have shown that $X_b(\xi)$ and $H(\xi)$ are coupled in a non-trivial fashion. We need to compute beforehand the topography profile $H(\xi)$ in the canonical domain. This depends on a non-trivial composition of the form $h(x(\xi, -D))$. This topographic composition is preprocessed using an iterative method as presented by Flamarion *et al.* (2019). The iterates are labelled by a superscript l . The iterative scheme has the following structure:

$$\left. \begin{aligned} X_b^l(\xi) &= \xi + \mathcal{C}_{k \neq 0} \left[\mathbf{F}^{-1} \left[\frac{\widehat{H}^l}{\cosh^2(kD)} \right] \right] + \mathbf{F}^{-1} \left[i \tanh(kD) \widehat{H}^l \right], \\ H^{l+1}(\xi) &= h(X_b^l(\xi)), \end{aligned} \right\} \quad (3.6a,b)$$

where the initial step is based on the identities $X_b^0(\xi) = \xi$ and $H^1(\xi) = h(\xi)$. The stopping criterion used is

$$\max_{\xi \in [-L/2, L/2)} |H^{l+1}(\xi) - H^l(\xi)| < \varepsilon,$$

where ε is a given tolerance. In our simulations, we used $\varepsilon = 10^{-12}$.

When we have a travelling wave along the free surface, the pathlines are identical to the streamlines. When this is not the case, one can still compute the streamlines. The potential's harmonic conjugate ψ is readily available from the Fourier representation (2.14*b*).

In the moving frame we have that

$$X = x - ct \quad \text{and} \quad Y = y, \quad (3.7a,b)$$

where c is the wave speed given by (2.6). The streamfunction ψ_T is obtained by putting $\tilde{\psi}$ together with the shear flow in the form

$$\psi_T(X, Y, t) := \tilde{\psi}(X, Y, t) + \frac{\Omega Y^2}{2} + (F - c)Y. \quad (3.8)$$

At any instant of time, the streamfunction can be evaluated on a uniform grid in the canonical domain and mapped onto points in the physical domain in order to trace its level curves there. Yet, at each given time, we denote $\psi_T(t) \equiv \psi_T(X, Y, t)$ and consider $\|\psi_T(t)\|_1$ as its 1-norm evaluated on the computational grid.

4. Results

It is well known in the literature that stagnation points and a critical layer can be formed beneath a periodic travelling wave in the presence of vorticity (Teles da Silva & Peregrine 1988; Ehrnström & Villari 2008; Ehrnström *et al.* 2012; Vasan & Oliveras 2014; Nachbin & Ribeiro-Jr. 2017; Ribeiro-Jr. *et al.* 2017). There are different forms of finding the initial wave profile, depending whether we have in mind an irrotational (Nachbin & Ribeiro-Jr. 2014) or a rotational (Ribeiro-Jr. *et al.* 2017) surface travelling wave. See the references within these two papers.

In the present study, the waves are linear and dispersive, so we do not have a (non-monochromatic) travelling wave. Nevertheless, for weak dispersion, the propagating waves change shape very slowly. A right-propagating disturbance is obtained by preprocessing our desired wave profile over a flat bottom and keeping the right-going mode. The initial wave elevation is usually positioned at a reasonable distance from the bottom topography so that there the Jacobian is effectively equal to 1, and therefore $N(\xi, 0) = N_0(\xi) \equiv \bar{\zeta}(x, 0) = \bar{\zeta}_0(x)$. Hence the wave elevation representations in the canonical and physical domains are identical.

In the present study the periodic boundary condition is only for numerical purposes, namely for the Fourier spectral method. We consider wave disturbances localized in space which undergo reflection and transmission over a bottom variation of compact support. Hence, over the time interval of our simulations, no disturbances should be observed at the endpoints of our computational domain. We consider a tabletop modulated wavetrain localized in space, which resembles a periodic wave in its central region. The goal is to observe a Kelvin cat-eye structure which (locally) resembles that of periodic waves.

4.1. Wave–current interaction for a slowly varying wavetrain

We start with a tabletop wave profile of the form

$$N_0(\xi) = \alpha e^{-2(\sigma(\xi - \xi_0))^s} \cos(k(\xi - \xi_0)), \quad (4.1)$$

where $\alpha = 10^{-3}$, $\sigma = 6 \times 10^{-3}$, $s = 8$ and $k = 2\pi/50$. The very first simulation is for an unforced case (with $h(x) = 0$ and $P(x) = 0$) where the underlying current is such that $\Omega = -18$ and $F = -9$. The respective background flow is given by $\mathbf{U} = (-18y - 9, 0)$, as defined in (2.3). The dispersion is very weak in this case. The wave profile barely changes during the simulation. The streamfunction fluctuation was computed over a large time interval ($t \in [0, 340]$) corresponding to a propagation distance of approximately 60 wavelengths. We observed that $\Delta\psi(t) = \|\psi_T(t) - \psi_T(0)\|_1 / \|\psi_T(0)\|_1 < 10^{-6}$ at all times. Hence, over this time interval the level curves of the streamfunction are a good approximation for the pathlines. The vector field of (2.7) is effectively autonomous.

The initial phase portrait obtained from the streamfunction $\psi_T(0)$ is depicted in figure 2. The central region is typical of a phase portrait for a periodic travelling wave in the presence of constant vorticity (Ehrnström & Villari 2008; Wahlén 2009). The novelty here is that the wavetrain is effectively of compact support, rather than periodic as in the previous studies. The super-Gaussian envelope, which provides a tabletop pattern over the central region of the wavetrain, was designed so that we could observe a Kelvin cat-eye structure similar to periodic waves, as presented numerically by Teles da Silva & Peregrine (1988), Vasan & Oliveras (2014) and Ribeiro-Jr. *et al.* (2017). This is the case in the region located approximately within

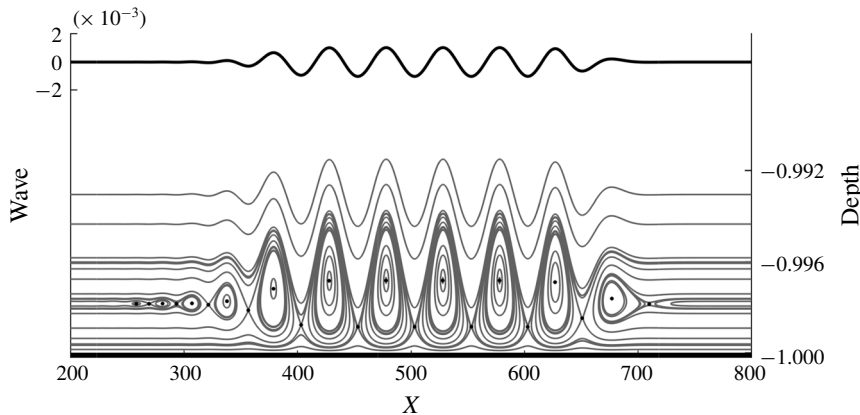


FIGURE 2. Nearly stationary regime depicting streamlines $\psi_T(0)$. Left vertical axis: the wave elevation scale (top thicker line). Right vertical axis: depth scale, indicating a Kelvin cat-eye structure very close to the bottom.

the interval [400, 600]. This is a first numerical display of the cat-eye structure dynamically adjusting to the endpoints of the wavetrain. The wave is propagating to the right and it is remarkable that, beneath the very small (weakly dispersive) oscillatory tail, the method can detect a number of diminishing cat-eyes (recirculation regions) fading to the left. The small asymmetry observed in the streamlines is due to the weak dispersion. On the left axis of figure 2 the small wave amplitude is quantified. The Kelvin cat-eye structure, generated by this linear wave, is narrow and located near the bottom, as indicated by the values on the right axis of figure 2. Nevertheless, due to a non-trivial vorticity the cat-eye structure is detached from the bottom, exhibiting both types of critical points: saddles and a centre. The cat-eye structure persists as the oscillatory tail of the wave changes and the recirculation regions adjust accordingly. In particular, in analogy with the development of an Airy-type solution, as the lagging oscillatory tail develops, a small new recirculation (cat-eye) region is generated.

4.2. Topographic forcing and the persistence of the cat-eye structure

Now we introduce a topography located in the middle of our computational domain. There is no pressure distribution along the free surface. The topography has compact support and a tabletop configuration, in order to locally resemble a periodic depth variation. The bottom profile is given by

$$h(x) = \delta e^{-2(\sigma(x-\tilde{x}_0))^s} \cos(k_b(x - \tilde{x}_0)), \quad (4.2)$$

where $\delta \ll 1$. The right-going initial wave profile is the same as before. We have kept the super-Gaussian (tabletop) modulation the same, for the wave and for the topography, so that they have comparable lengths. The physical domain is schematically depicted in figure 3. The initial disturbance has a Kelvin cat-eye structure formed beneath it and will eventually interact with the topography. At the same time, a wave is generated by the current topography interaction, as studied in Flamarion *et al.* (2019). We will examine the submarine pathline structure in the presence of all these features.

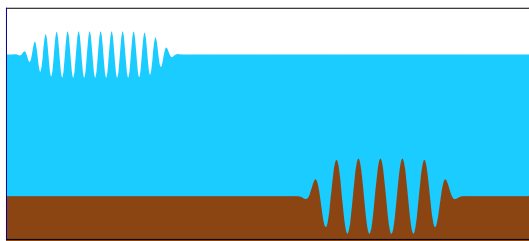


FIGURE 3. Schematic physical domain for the wave–topography interaction. Two regimes are considered: $\lambda \approx l$ and $\lambda \gg l$ (rapidly varying topography).

We consider two wave–topography regimes. First we consider the regime where the surface wavelength is comparable to that of the topography and we let $l/\lambda = 0.5$. Then we consider the case where the topography is rapidly varying: $l/\lambda = 0.05$. The parameters used for the underlying flow and the initial disturbance (4.1) are: $\Omega = -18$, $F = -9$, $\alpha = 10^{-3}$, $\sigma = 3 \times 10^{-3}$, $s = 8$ and $k = 2\pi/50$. For the topography we used $\delta = 2 \times 10^{-3}$, $k_b = 2k$ and $k_p = 20k$ in expression (4.2). The amplitude of the topography needs to be small so that the height of the waves generated by the current–topography interaction is also small, which is required in the approximation (2.17). For more details about the amplitude of generated waves in linear regimes, see Milewski (2004).

In order to visualize the pathlines we track the orbits of cloud tracers, each tracer solving the dynamical system (3.1). In figure 4 we consider the $l/\lambda = 0.5$ case, first in the (fixed) laboratory frame. In the top snapshot (at time $t = 34$) we see the initial (right-going) disturbance at the left of the topography and the current-generated wave above the topography. We focus on the initial disturbance and release cloud tracers below this wave. The initial cloud (depicted by black particles near the bottom) is positioned to the left of $x = 500$. At time $t = 34$ the cloud has travelled to the right, positioned below the wave train, and is depicted by a bunch of white particles. The inset provides a zoom of a white cloud with the tracers' initial positions. In the wave's moving frame, their non-stationary evolution will trace closed pathlines, which display the time-dependent Kelvin cat-eye structure. The interaction of this structure with the topography is shown in figure 4(b). At time $t = 118$ we observe the pathlines in a terrain-following pattern, moving over the topography. The particle trajectories are distorted by the bottom undulations. At this stage the right-going initial wave has a linear interaction with the stationary wave generated by the current–topography mechanism. The computational domain is wider than that shown by these pictures. The wave pattern due to the current–topography interaction is in accordance with that observed in Flamarion *et al.* (2019), where there were standing waves above the topography together with waves moving downstream. In figure 4(c) at time $t = 170$ the initial right-going disturbance is leaving the variable bottom region. The inset shows the tracers back to (nearly) the same formation as at time $t = 34$.

The wave profile, due to the initial disturbance (4.1), changes very slowly. Hence we proceed as with travelling waves and display particle orbits in the moving frame associated with the wave speed c , given in (2.6). In figure 5 the Kelvin cat-eye structure is evident, with closed pathlines forming a recirculation region about the stagnation point. In figure 5(a), the inset displays tracers that were initially located at the black dots, but have moved along the cat-eye contours reaching the white dots at time $t = 34$. In figure 5(b), at time $t = 118$, the inset displays material curves, where a collection of tracers is following a given contour of the cat-eye structure. In the

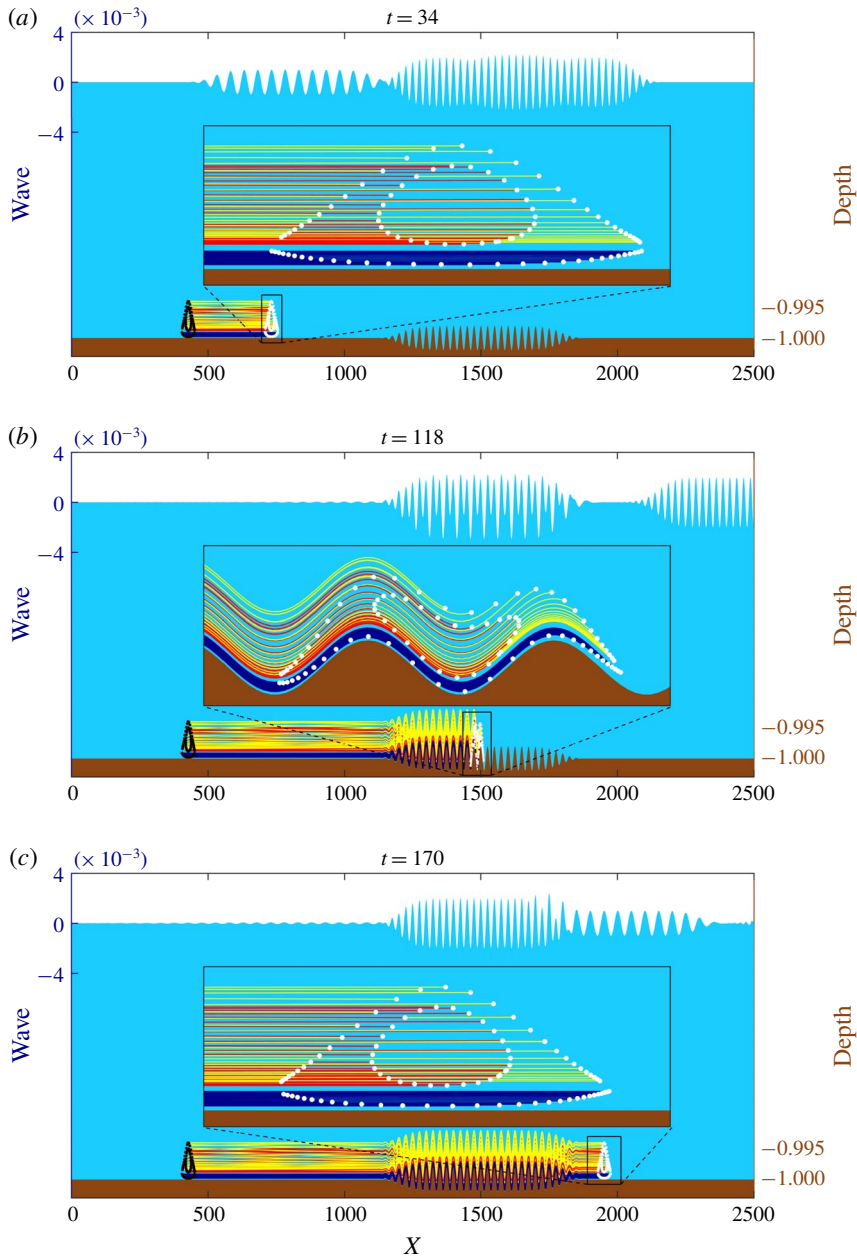


FIGURE 4. Tracer pathlines in the laboratory frame, with $\lambda = 2l$: initial tracer positions (black dots) and final tracer positions (white dots). Left axis: scale for the free surface disturbance. Right axis: depth values for the tracers near the bottom. An animation (movie 1) may be found in the supplementary material for this article, which is available at <https://doi.org/10.1017/jfm.2020.51>.

middle part (in red) we have a closed material curve where the white points indicate the current position of each tracer. We have the same particles (cloud of tracers) in

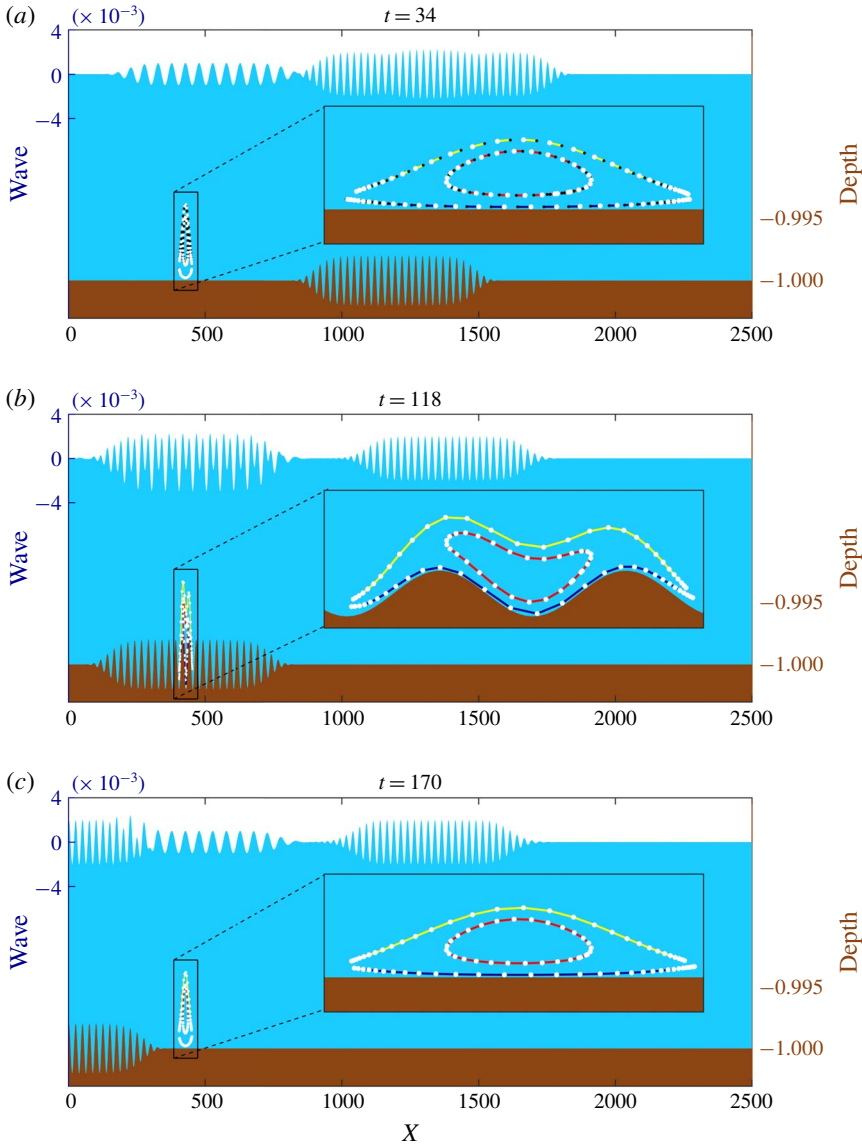


FIGURE 5. Tracer pathlines in the moving frame, with $\lambda = 2l$: initial tracer positions (black dots) and final tracer positions (white dots). Left axis: scale for the free surface disturbance. Right axis: depth values for the tracers near the bottom. The persistence of Kelvin cat-eye structure is accurately captured in time, as it adjusts to the topography. An animation (movie 1) may be found in the supplementary material for this article.

all snapshots of figure 5. The top material curve (in yellow) and the bottom material curve (in blue) eventually connect to the saddle points, as were displayed in figure 2. The Kelvin cat-eye structure is persistent and the respective critical layer evolves accordingly.

We now consider a rapidly varying topography, as displayed in figure 6. The initial disturbance and cloud of markers are the same as in the previous example. The

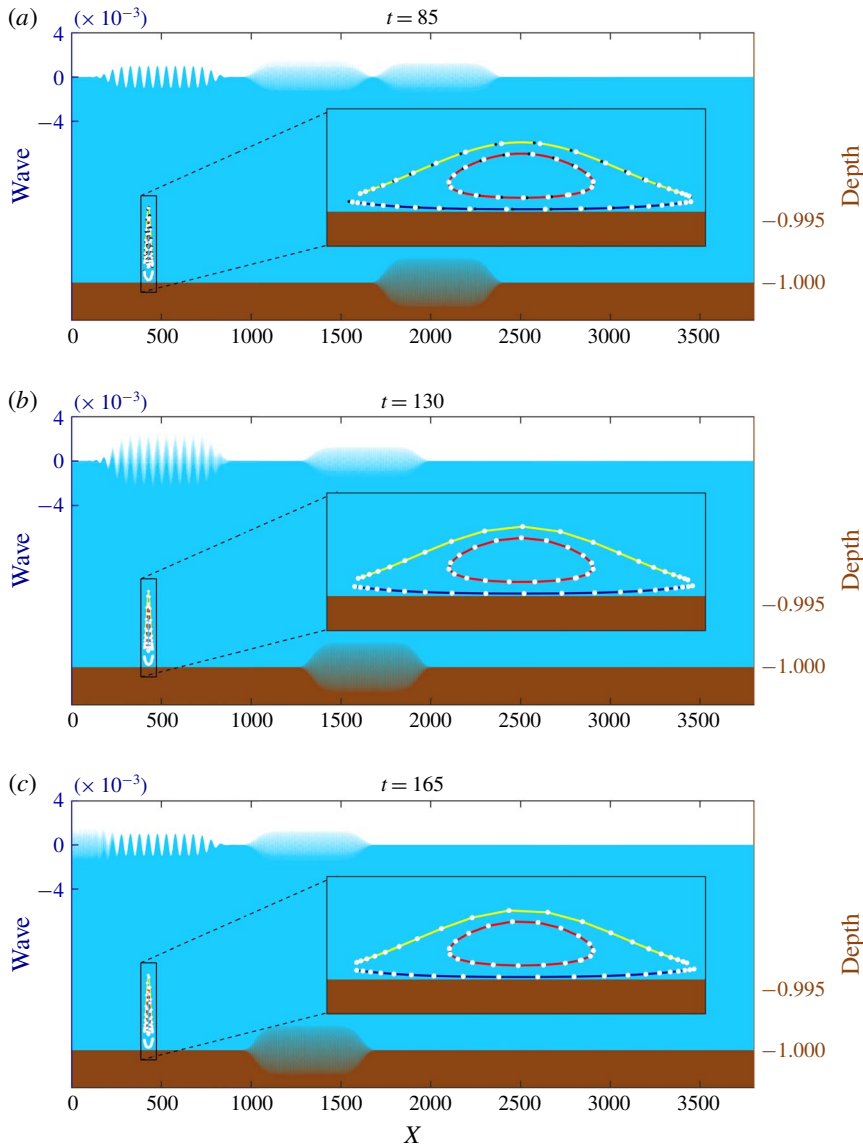


FIGURE 6. Tracer pathlines in the moving frame; rapidly varying topography case ($\lambda \gg D$): initial tracer positions (black dots) and final tracer positions (white dots). Left axis: scale for the free surface disturbance. Right axis: depth values for the tracers near the bottom. For panels (b) and (c) we erased the initial position for a better visualization of the cat-eye.

current–topography interaction generates rapidly varying wavetrains. In the present regime there is a stationary wavetrain above the topography and another wavetrain moving upstream. As the wavetrain propagates over the rapidly varying topography, the cat-eye structure is destroyed. In figure 7(a) we observe the disintegration of the material curves, which formed the contours of the cat-eye. But as soon as the wavetrain reaches the other side of the topography, it is remarkable to observe that

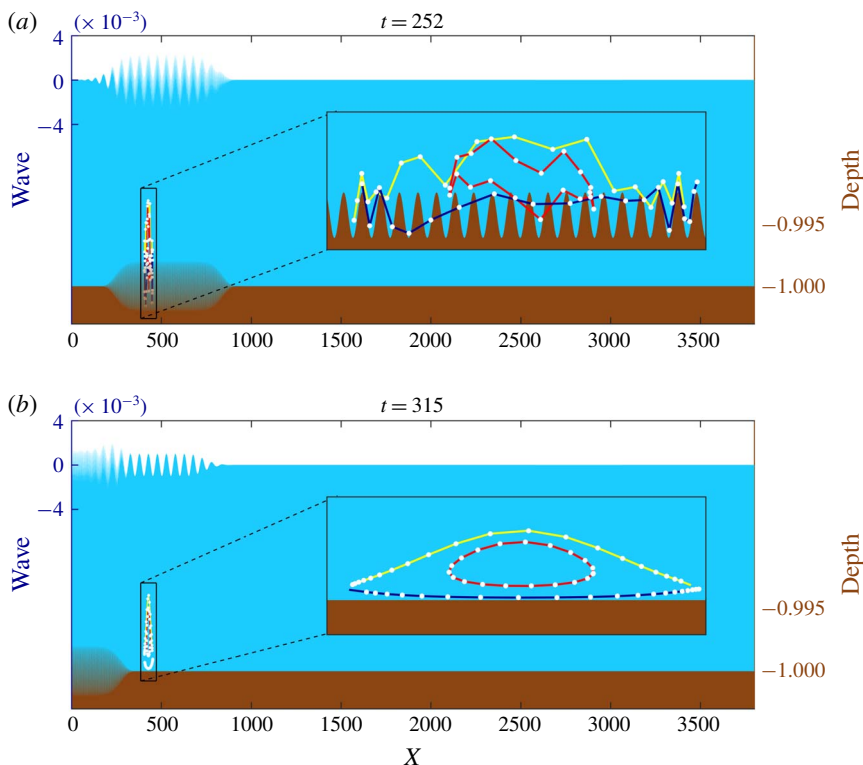


FIGURE 7. The right-going wave, from figure 6, crosses over the rapidly varying topography. The bottom's fine features destroy the cat-eye configuration. Upon leaving the variable-depth region, a cat-eye is immediately reformed with the same particles as considered in figure 6.

each respective group of markers remain, forming a closed material curves of a cat-eye (recirculation) region. It is important to comment that the collision of waves propagating in opposite directions had a minor effect since we are dealing with linear waves. With nonlinear waves the scenario can be much more complicated, also due to the possibility of wave breaking. It is of interest to investigate the evolution of the Kelvin cat-eye structure in such a case, but that is beyond the scope of the present study.

4.3. The onset of a Kelvin cat-eye structure

4.3.1. Due to current–topography interaction

Up to this point we had tracers released beneath the initial wave disturbance. This initial wave disturbance immediately establishes the submarine phase-plane picture as seen in figure 2. In the present case, the free surface starts at rest. We then compute the submarine orbits for tracers placed beneath the wave generated by the current–topography interaction. At time $t=0^+$ there are no waves on the surface nor stagnation points in the bulk. The flow and topographic parameters are the same as before, but $k_b = k$.

At time $t=0$ we distribute tracers at positions that would correspond to a cat-eye. This is shown in figure 8(a). Then a standing wave appears, and at time $t = 10$

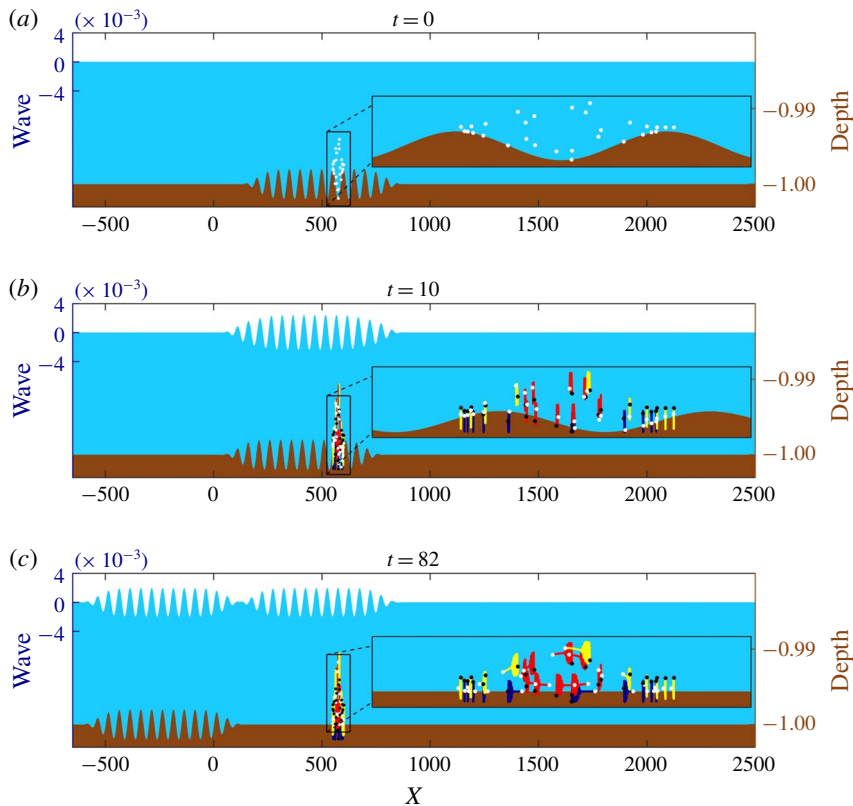


FIGURE 8. The onset of the Kelvin cat-eye structure in the wave's moving frame ($\lambda = l$): initial tracer position (black dots) and final tracer position (white dots). (a) At $t=0$: tracers are positioned in a cat-eye formation before the simulation starts. (b) At $t=10$: onset of tracer motion. (c) At $t=82$: the onset of the cat-eye formation is captured. Left axis: scale for the free surface disturbance. Right axis: depth values for the tracers near the bottom. An animation (movie 2) may be found in the supplementary material for this article.

we observe the tracers moving up and down (figure 8b). The colour code (see online version) is the same as before, according to the position along the cat-eye. Eventually a downstream-propagating wavetrain is generated by the topography. Note that the cloud of tracers is always centred about the same position because we are in the moving frame with respect to this wave. Therefore, the topography seems to be moving to the left. Observe that, after time $t = 82$ the tracers are beneath an effectively steady wave. In this moving region the velocity field is nearly autonomous. After a preliminary vertical oscillation, the markers initiate tracing orbits in the anticlockwise direction, revealing a cat-eye configuration as clearly seen a later times in figure 9. The initial part of the pathlines was omitted for a better visualization.

4.3.2. Due to a variable pressure distribution

In order to study the natural emergence of a critical layer, Johnson (2012) suggests a pressure distribution along the surface. As in a storm-surge-like scenario, we apply

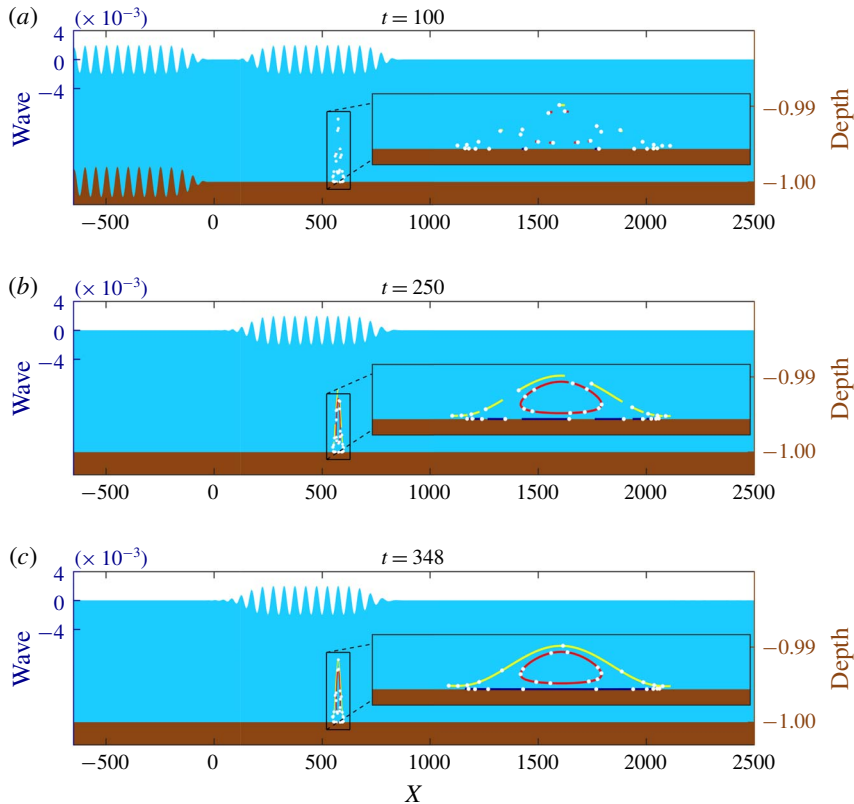


FIGURE 9. Continuation from figure 8. The pathlines are restarted for a better visualization. As time evolves we clearly see the Kelvin cat-eye structure. An animation (movie 2) may be found in the supplementary material for this article.

a localized low pressure distribution

$$P(x) = -0.2e^{-\sigma x^2}$$

along the free surface at time $t > 0$. The bottom is flat ($h(x) = 0$) and the free surface initially undisturbed ($N_0(\xi) = 0$, $\Phi(\xi, 0) = 0$). The underlying shear flow is such that $\Omega = -18$ and $F = -9$.

In figure 10 we display different stages of the submarine dynamics, in a reference frame where the pressure is stationary. In figure 10(a), when the pressure distribution is about to be applied, a cloud of tracers is prepared within the fluid body. At time $t = 7$ the steady pressure distribution has generated a steady pulse-shaped wave and two depression waves, which are about to propagate to the left and right respectively. The pathlines are quite developed, beneath the steady wave, as depicted in figure 10(c,d). The white dots indicate the final tracer position for the respective time interval.

We have a single cat-eye (recirculation) region, located below the pressure disturbance. As mentioned in the Introduction, the critical layer is defined by having recirculation regions containing closed pathlines and separating the fluid into two

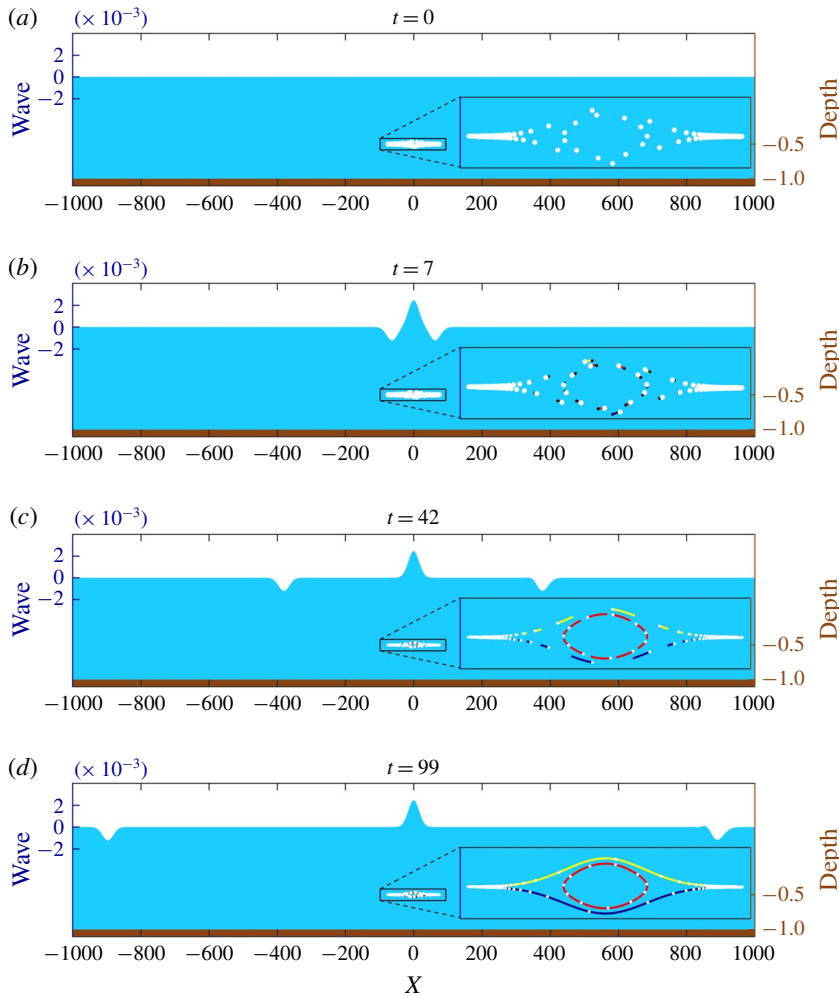


FIGURE 10. The onset of a Kelvin cat-eye due to a localized pressure distribution. (a) Markers initially positioned to capture the cat-eye formation. From time $t = 7$ until time $t = 99$ the cat-eye is clearly traced by the particle pathlines. Left axis: scale for the free surface disturbance. Right axis: depth values for the tracers near the bottom. An animation (movie 3) may be found in the supplementary material for this article.

disjoint regions. In the present case, we have nearly horizontal stagnation lines emerging from both sides of the cat-eye pattern. Above this line the flow is in one direction, while below it has a reversed direction. The velocity field is continuous so there is no velocity jump across the stagnation segment. This scenario has not been reported before, in particular for a non-stationary wave regime under forcing. As pointed out by a referee, the recent (unpublished) work by Chen, Walsh & Wheeler (2019) also displays a single (but half) cat-eye structure. Their configuration is quite different: one has two fluids of different densities bounded by two walls. Hence there are no surface waves. The free surface is the interface between the two fluids where there is a vorticity jump, different from our smooth transition. The bottom layer is

irrotational. Figure 1 of their manuscript displays a schematic picture of what the authors call an internal bore (in the upper layer) with a ‘half cat’s eye streamline pattern’.

5. Conclusions

We have studied linear non-stationary rotational surface waves, in the presence of constant vorticity. We consider the regime where the Kelvin cat-eye structure can be observed. In the linear regime one has a very narrow structure near the bottom. The accurate numerical method captured all details of the cat-eye structure and the respective critical layer separating left- from right-going streams. Particle trajectories were computed and visualized by evolving the respective submarine dynamical system with a cloud of tracers. The accurately computed pathlines permitted animations (movies 1, 2 and 3) presented as supplementary material. These include the formation of a Kelvin cat-eye structure arising from an initially undisturbed surface. Waves were generated from either the current–topography interaction or by a surface pressure distribution suddenly imposed.

Acknowledgements

The work of M.V.F. was supported in part by CNPq-Science without Borders under (PDE) 200920/2014-6 and by CNPq-Cotas do Programa de Pós-Graduação (GM/GD) 140773/2014-2. The work of A.N. was supported in part by CNPq under (PQ-1B) 304671/2017-7 and FAPERJ Cientistas do Nosso Estado project no. E-26/203.023/2017. R.R.J. is grateful to IMPA for the research support provided during the Summer Programme of 2018 and to the University of Bath for an extended visit to the Department of Mathematical Sciences. A.N. and R.R.-Jr. thank Professor R. Johnson for his comments during their visits to Vienna. A.N. is grateful to the Erwin Schrödinger International Institute for Mathematics and Physics for support and hospitality during the ESI Programme on ‘Mathematical Aspects of Physical Oceanography’. R.R.-Jr. thanks Professor A. Constantin for his support and hospitality during his visit to the Department of Mathematics of the University of Vienna. The authors are grateful to all three referees for their thorough reviews and comments that improved this article.

Declaration of interests

The authors report no conflict of interest.

Supplementary movies

Supplementary movies are available at <https://doi.org/10.1017/jfm.2020.51>.

REFERENCES

- AASEN, A. & VARHOLM, K. 2018 Traveling gravity water waves with critical layers. *J. Math. Fluid Mech.* **20**, 161–187.
- BUHLER, O. 2009 *Waves and Mean Flows*. Cambridge University Press.
- CHEN, R. M., WALSH, S. & WHEELER, M. 2019 Center manifold without a phase space for quasilinear problems in elasticity, biology and hydrodynamics. [arXiv:1907.04370v1](https://arxiv.org/abs/1907.04370v1).

- CONSTANTIN, A. 2011 *Nonlinear Water Waves with Applications to Water–Current Interactions and Tsunamis*, CBMS-NSF Regional Conference Series in Applied Mathematics, vol. 81. SIAM.
- CONSTANTIN, A. 2017 Nonlinear water waves: introduction and overview. *Phil. Trans. R. Soc. Lond. A* **376** (2111), 20170310.
- CONSTANTIN, A., STRAUSS, W. & VARVARUCA, E. 2016 Global bifurcation of steady gravity water waves with critical layers. *Acta Math.* **217**, 195–262.
- CONSTANTIN, A. & VILLARI, G. 2008 Particle trajectories in linear water waves. *J. Math. Fluid Mech.* **10**, 1–18.
- EHRNSTRÖM, M., ESCHER, J. & VILLARI, G. 2012 Steady water waves with multiple critical layers: interior dynamics. *J. Math. Fluid Mech.* **14**, 407–419.
- EHRNSTRÖM, M. & VILLARI, G. 2008 Linear water waves with vorticity: rotational features and particle paths. *J. Differ. Equ.* **244**, 1888–1909.
- FLAMARION, M. V., MILEWSKI, P. A. & NACHBIN, A. 2019 Rotational waves generated by current–topography interaction. *Stud. Appl. Maths* **142**, 433–464.
- FRANCIUS, M. & KHARIF, C. 2017 Two-dimensional stability of finite-amplitude gravity waves on water of finite depth with constant vorticity. *J. Fluid Mech.* **830**, 631–659.
- HENRY, D. 2013 Steady periodic waves bifurcating for fixed-depth rotational flows. *Q. Appl. Maths* **LXXI** (3), 455–487.
- JOHNSON, R. S. 1986 On the nonlinear critical layer below a nonlinear unsteady surface wave. *J. Fluid Mech.* **167**, 327–351.
- JOHNSON, R. S. 2012 Models for the formation of a critical layer in water wave propagation. *Phil. Trans. R. Soc. Lond. A* **370**, 1638–1660.
- KO, J. & STRAUSS, W. 2008 Large-amplitude steady rotational water waves. *Eur. J. Mech. (B/Fluids)* **27**, 96–109.
- MILEWSKI, P. A. 2004 The forced Korteweg-de Vries equation as a model for waves generated by topography. *CUBO Math. J.* **6**, 33–51.
- MILEWSKI, P. A. & TABAK, E. G. 1999 A pseudo-spectral algorithm for the solution of nonlinear wave equations. *SIAM J. Sci. Comput.* **21** (3), 1102–1114.
- NACHBIN, A. 2003 A terrain-following Boussinesq system. *SIAM J. Appl. Maths* **63**, 905–922.
- NACHBIN, A. & RIBEIRO-JR., R. 2014 A boundary integral formulation for particle trajectories in Stokes waves 2014. *Discrete Continuous Dyn. Syst. A* **34** (8), 3135–3153.
- NACHBIN, A. & RIBEIRO-JR., R. 2017 Capturing the flow beneath water waves. *Phil. Trans. R. Soc. Lond. A* **376** (2111), 20170098.
- RIBEIRO-JR., R., MILEWSKI, P. A. & NACHBIN, A. 2017 Flow structure beneath rotational water waves with stagnation points. *J. Fluid Mech.* **812**, 792–814.
- SOONTIENS, N., SUBICH, C. & STASTNA, M. 2010 Numerical simulation of supercritical trapped internal waves over topography. *Phys. Fluids* **22**, 16605.
- TELES DA SILVA, A. F. & PEREGRINE, D. H. 1988 Steep, steady surface waves on water of finite depth with constant vorticity. *J. Fluid Mech.* **195**, 281–302.
- TREFETHEN, L. N. 2001 *Spectral Methods in MATLAB*. SIAM.
- VASAN, V. & OLIVERAS, K. 2014 Pressure beneath a traveling wave with vorticity constant. *Discrete Continuous Dyn. Syst. A* **34** (8), 3219–3239.
- WAHLÉN, E. 2009 Steady water waves with a critical layer. *J. Differ. Equ.* **246**, 2468–2483.